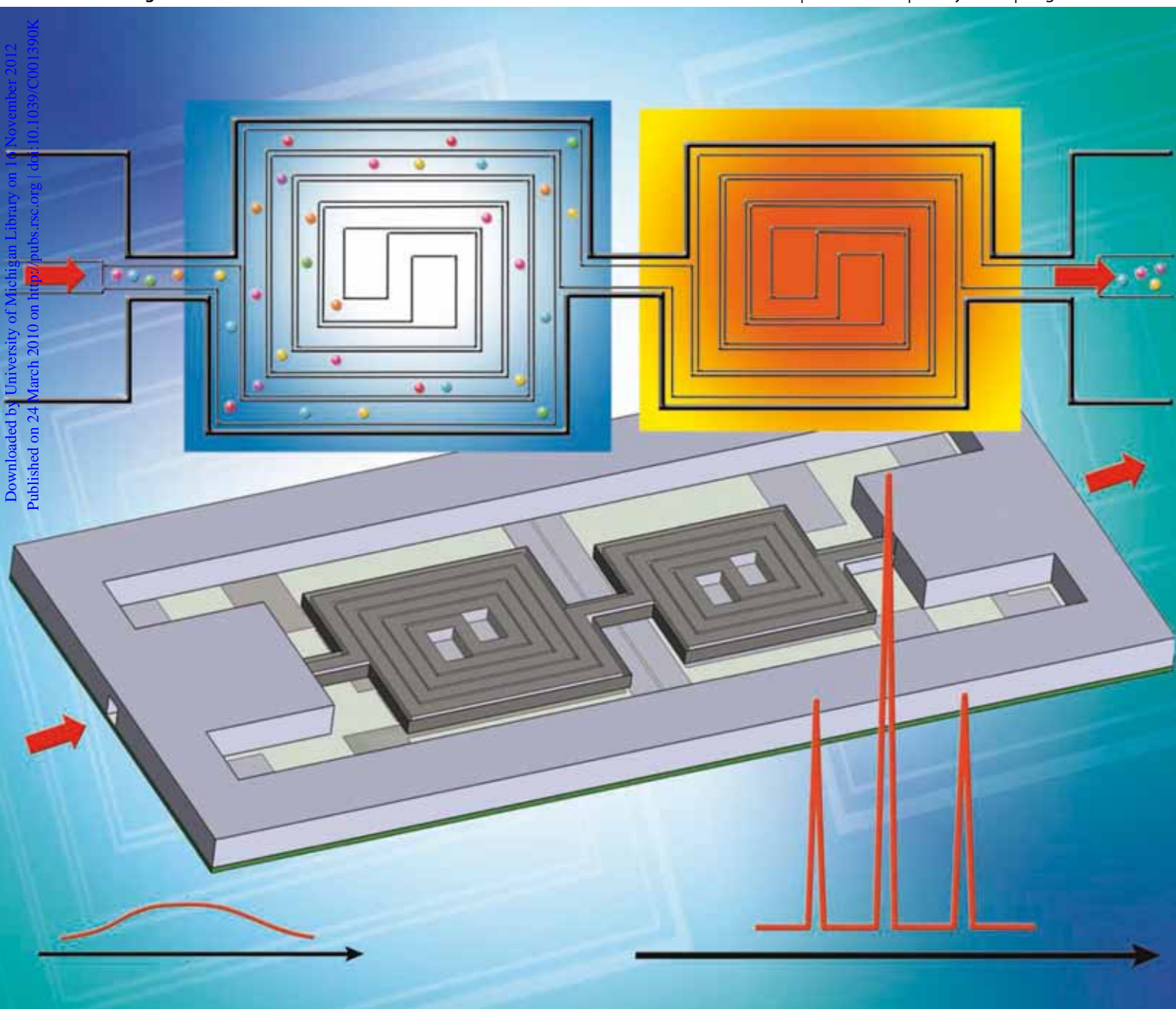


Lab on a Chip

Micro- & nano- fluidic research for chemistry, physics, biology, & bioengineering

www.rsc.org/loc

Volume 10 | Number 13 | 7 July 2010 | Pages 1633–1740



Downloaded by University of Michigan Library on 16 November 2012
Published on 24 March 2010 on <http://pubs.rsc.org> | doi:10.1039/C001390K

ISSN 1473-0197

RSC Publishing

Kurabayashi
2D micro gas chromatography

Ho
Continuous sorting of embryoid
bodies



1473-0197(2010)10:13;1-7

Microfabricated thermal modulator for comprehensive two-dimensional micro gas chromatography: design, thermal modeling, and preliminary testing†

Sung-Jin Kim,^{ab} Shaelah M. Reidy,^{ac} Bruce P. Block,^{ad} Kensall D. Wise,^{ac} Edward T. Zellers^{aef} and Katsuo Kurabayashi^{*abc}

Received 21st January 2010, Accepted 26th February 2010

First published as an Advance Article on the web 24th March 2010

DOI: 10.1039/c001390k

In comprehensive two-dimensional gas chromatography (GC×GC), a modulator is placed at the juncture between two separation columns to focus and re-inject eluting mixture components, thereby enhancing the resolution and the selectivity of analytes. As part of an effort to develop a μ GC× μ GC prototype, in this report we present the design, fabrication, thermal operation, and initial testing of a two-stage microscale thermal modulator (μ TM). The μ TM contains two sequential serpentine Pyrex-on-Si microchannels (stages) that cryogenically trap analytes eluting from the first-dimension column and thermally inject them into the second-dimension column in a rapid, programmable manner. For each modulation cycle (typically 5 s for cooling with refrigeration work of 200 J and 100 ms for heating at 10 W), the μ TM is kept approximately at $-50\text{ }^{\circ}\text{C}$ by a solid-state thermoelectric cooling unit placed within a few tens of micrometres of the device, and heated to $250\text{ }^{\circ}\text{C}$ at $2800\text{ }^{\circ}\text{C s}^{-1}$ by integrated resistive microheaters and then cooled back to $-50\text{ }^{\circ}\text{C}$ at $250\text{ }^{\circ}\text{C s}^{-1}$. Thermal crosstalk between the two stages is less than 9%. A lumped heat transfer model is used to analyze the device design with respect to the rates of heating and cooling, power dissipation, and inter-stage thermal crosstalk as a function of Pyrex-membrane thickness, air-gap depth, and stage separation distance. Experimental results are in agreement with trends predicted by the model. Preliminary tests using a conventional capillary column interfaced to the μ TM demonstrate the capability for enhanced sensitivity and resolution as well as the modulation of a mixture of alkanes.

Introduction

Comprehensive two-dimensional gas chromatography (GC×GC) is an analytical technique used to separate and detect the components of complex mixtures of volatile organic compounds.^{1–3} Unlike standard GC, which uses a single column for vapor separation, GC×GC couples a first-dimension column to a relatively short second-dimension column whose retention properties are complementary to those of the first-dimension column. Through a junction-point modulator between the two columns (Fig. 1A), mixture components separated on the first-dimension column are focused and reinjected as a series of narrow pulses onto the second-dimension column. This results in

an increase in peak capacity (*i.e.*, the number of compounds that can be separated in a given analysis) and in sensitivity as a 2-D chromatogram is produced.^{1–3}

A pneumatic^{4,5} or thermal^{6–14} modulator (TM) is used at the interface between the two columns, with the latter generally providing a greater degree of sensitivity enhancement. A TM relies on low temperature to trap and focus the analytes as they elute from the first-dimension column, and then reintroduces them to the second-dimension column by rapid heating. By repeating this operation in rapid succession, the vapor profile is parsed into several segments, each of which is eluted through the second-dimension column. TMs, which are used in conventional bench-scale GC×GC systems, can be grouped into a thick stationary-phase film modulator and a cryogenic modulator. In the former, analytes are focused in a small section of capillary by the polymeric phase at ambient temperature.^{6,7} The latter uses a cryogenically cooled fluid such as CO_2 , N_2 , or air.^{8–14} The two types of modulators commonly use conductive or convective heating techniques to rapidly raise the temperature of the modulator. However, those macro-scale TMs relying on cryogenically cooled fluids are resource intensive^{8–12} and/or demand a large amount of refrigeration work (*e.g.*, $\sim 10\text{ kJ}$ for a cooling cycle of $\sim 5\text{ s}$).¹³ Furthermore, power dissipation for typical heating devices can be on the order of 1 kW.^{6,7,13,14}

Numerous efforts have been made to develop GC prototypes containing microfabricated components (μ GC).^{15–27} These miniaturized systems^{16–20} and their components^{21–27} can operate at relatively low power; however, the lengths of the columns

^aThe Engineering Research Center for Wireless Integrated Microsystems (WIMS), University of Michigan, Ann Arbor, MI 48109, USA

^bDepartment of Mechanical Engineering, University of Michigan, Ann Arbor, MI 48109, USA. E-mail: katsuo@umich.edu; Fax: +1-734-647-3170; Tel: 1-734-615-5211

^cDepartment of Electrical Engineering and Computer Science, University of Michigan, Ann Arbor, MI 48109, USA

^dDepartment of Atmospheric, Oceanic, and Space Science, University of Michigan, Ann Arbor, MI 48109, USA

^eDepartment of Environmental Health Sciences, University of Michigan, Ann Arbor, MI 48109, USA

^fDepartment of Chemistry, University of Michigan, Ann Arbor, MI 48109, USA

† Electronic supplementary information (ESI) available: Figures of microfabrication process and temperature calibration, as well as derivation of equations for the lumped thermal model. See DOI: 10.1039/c001390k

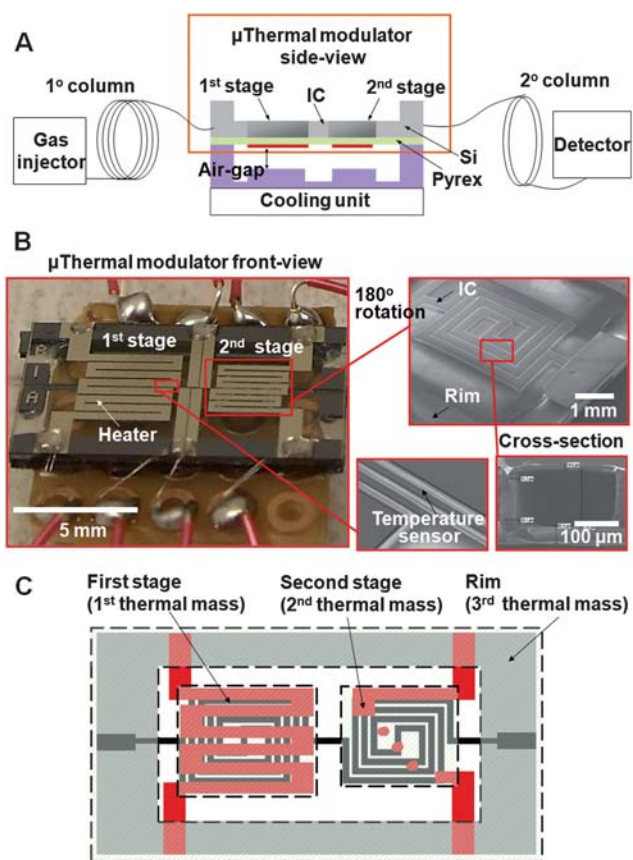


Fig. 1 Miniaturized thermal modulator (μ TM). (A) Schematic of GC \times GC system incorporating the μ TM. Key components of the μ TM are two-stage silicon-microchannels, a Pyrex membrane, and interconnection channels (ICs). A Si-spacer maintains the air-gap between the μ TM and the cooling unit. The cooling unit has a thermoelectric cooler and a fan cooler. The thermoelectric cooler keeps the temperature of the μ TM approximately at -55°C when there is no heating in the μ TM stages. We vary the size of the Pyrex membrane, the air gap, and the IC to explore the optimal device performance. (B) Photographs of μ TM. Each stage has serpentine microchannels ($250\ \mu\text{m}$ -width and $140\ \mu\text{m}$ -depth) on its back side, on-chip microheaters and temperature sensors on its front side. The microchannel lengths on the first and second stages are $4.2\ \text{cm}$ and $2.8\ \text{cm}$, respectively. A rim structure is used to reinforce the mechanical strength of the μ TM. (C) Control volumes for the lumped thermal model. Each thermal mass includes the Si layer and the corresponding Pyrex membrane area.

employed are inherently limited, with typical columns ranging in length from 0.5 to 3 metres.^{20–26} Accordingly, this places an inherent limit on the peak capacity. A μ GC system incorporating two-dimensional gas chromatography (*i.e.*, μ GC \times μ GC) is a promising approach to overcome this limitation. Although a preliminary report has recently been described on the use of pneumatic modulation in a μ GC \times μ GC system,²⁸ there has yet to be a report on a microfabricated TM (μ TM) for μ GC \times μ GC applications. To be effective, the μ TM must span a broad range of temperature (*e.g.* -50 to 250°C) at a very high rate ($>1000^\circ\text{C s}^{-1}$, ideally during both heating and cooling).

In this article, we report on the design, fabrication, modeling, and preliminary testing of a μ TM (Fig. 1B) that incorporates two series-coupled serpentine Pyrex-on-Si microchannels (stages)

that are sequentially cooled to trap and focus vapors and then heated to desorb them. We adopt two-stage modulation where analytes trapped in the first stage are thermally released into the (cooled) second stage for additional focusing prior to injection into the second-dimension column. In addition, the second stage is not heated until the first stage has cooled to a temperature sufficient for trapping. This alternating heating and cooling of each stage helps to avoid ‘breakthrough’, whereby a sample is lost due to incomplete trapping during thermal transitions, which is a potential problem with single-stage modulator designs.¹³ An emphasis is placed on three critical design parameters that govern the heat capacity of the device structure and the rate at which heat energy is transported between stages and from each stage to the environment: (1) the thickness of the Pyrex membrane that seals the silicon microchannels of the μ TM; (2) the air gap between the cooling unit and the μ TM; and (3) the interconnection channel (IC) that connects the two stages and the rim. We explore the effects of varying these parameters on the device performance using a lumped heat transfer model, where the trade-off between the heating-cooling cycle speed and the power requirement as well as the thermal crosstalk between the two stages are carefully considered. Preliminary results demonstrating the modulation of a single compound and a simple mixture of compounds are presented.

Experimental

Microfabrication and assembly

The fabrication process is summarized in Fig. S1 of the electronic supplementary information (ESI).† The first and second stages of the μ TM consist of meander-line boron-doped-Si microchannels 4.2 and $2.8\ \text{cm}$ long, respectively, with cross-sectional dimensions of $250\ (\text{w}) \times 140\ (\text{h})\ \mu\text{m}$ and a wall thickness of $30\ \mu\text{m}$. The IC has the same cross section and wall thickness, and consists of three segments: two that connect each stage to the rim and one that connects the two stages. The three IC segments had the same length, which was varied from $0.5\ \text{mm}$ to $1.5\ \text{mm}$ in different device designs. Anodically bonded Pyrex glass, either 40 or $100\ \mu\text{m}$ thick, was used to seal the microchannels. Microheaters and temperature sensors made of Ti/Pt were patterned on the Pyrex membrane. Microfabricated Si spacers, used to create an air gap (22 – $63\ \mu\text{m}$) between the μ TM and the top surface of the thermoelectric cooler (SP2394, Marlow industries, www.marlow.com), were precisely aligned with a microscope and bonded with an epoxy adhesive onto the Pyrex membrane; the Si spacers were separately fabricated by a two-step silicon deep reactive ion etching process. Then the μ TM was mounted on a printed circuit board and wire bonded for electrical connection.

A thin layer of thermally conductive paste was used to ensure good thermal contact between the Si spacers and the thermoelectric cooler. With a height gauge (Series 192, Mitutoyo, www.mitutoyo.com), the μ TM with Si spacers was manually aligned and bonded to the cooling unit. A small axial fan (E1U-N7BCC-03, SundialMicro, www.sundialmicro.com) facilitated heat transfer from the backside of the thermoelectric cooler. Finally, a custom-made chamber was used to seal the μ TM.

Stationary-phase coating of the μ TM

Deactivated fused-silica capillaries having 250 μm i.d. and 100 μm i.d. were inserted in the inlet and outlet ports, respectively, of the μ TM and secured with high-temperature epoxy (Hysol 1C, Dexter Corp., www.rshughes.com) to form a leak free seal. The internal walls of the μ TM microchannels were dynamically coated with polydimethylsiloxane (PDMS, OV-1, Ohio Valley, www.ovsc.com) from a solution (0.10 g mL⁻¹ in 1 : 1 pentane–dichloromethane) that also contained a thermally activated cross-linking agent, dicumyl peroxide (1 mg mL⁻¹, Aldrich, www.sigmaaldrich.com).²⁴ Dynamic coating entails applying a positive pressure of nitrogen gas to a reservoir containing the polymer solution and directing it through the device. Nitrogen flow was maintained for 2 h after the solution passed through the device to evaporate the solvent. Cross-linking was achieved by temporarily sealing the inlet and outlet ports of the μ TM and heating to 180 °C with the integrated heaters. Although the short capillary sections connected to the device are also coated during this process, they do not affect the device performance or the chromatographic separation of the analytes significantly.

Temperature control

The temperature sensors were calibrated by placing the μ TM in a convection oven, which provided a temperature range of –60 to 120 °C (see ESI, Fig. S2†). Heating was achieved by applying a square-wave voltage pulse to the microheater on each μ TM stage using separate DC power supplies (E3646A, Agilent). A custom-made computer program (C#, Microsoft) controlled the heating operation. Constant power of 40 W (8 A and 5 V) was continuously applied to the thermoelectric cooler. Thus, one stage was maintained at low temperature as the other stage was heated. Dry air or nitrogen was used to prevent moisture condensation on the μ TM surface.

Peak modulation conditions

The μ TM was placed in the oven of a bench-scale GC (7890A, Agilent, Santa Clara, CA) equipped with a split/splitless injector and a flame-ionization detector (FID). A 3-m-long section of a commercial fused-silica capillary column (250 μm i.d.) having a PDMS stationary phase (0.25 μm thickness) was connected to the short section of capillary remaining at the device inlet by means of a press-fit connector. In lieu of a second-dimension column, the outlet of the μ TM was connected to the FID with a short length of uncoated, deactivated fused silica capillary (100 μm i.d.), also by means of a press-fit connector.

The linear velocity of the He carrier gas was set to 12 cm s⁻¹ by adjusting the head pressure on the GC inlet and measuring the time required for a sample of methane gas (unretained) to pass through the system. Headspace samples (1 μL) of reagent-grade n-alkanes (Sigma-Aldrich) were injected with a nominal split ratio of 100 : 1. Separations were performed with the GC oven set at 30 °C. Modulation was achieved by applying 100-ms voltage pulses to each stage in succession, with a 1-sec delay between first and second stage heating, which raised the temperature of each stage to 250 °C. The period of time between modulations was either 5 s or 7 s. The sampling rate of the detector was 500 Hz.

Results and discussion

Energy-change rates

We developed a heat transfer model to predict the thermal responses and the extent of thermal crosstalk between the stages of the μ TM. The governing equations were obtained from a balance among energy rates (unit: W), accounting for changes in energy storage and heat transfer due to conduction, natural convection, and radiation. Because of the high thermal conductivity of the silicon channels and the thin layer of the Pyrex membrane, we used the lumped thermal model for each stage and the rim (Fig. 1C).²⁹ The equations are coupled as follows (see ESI for detailed derivation†):

$$\dot{E}_{1\text{-sys}} = \dot{E}_{1\text{-TEC}} + \dot{E}_{1-3} + \dot{E}_{1-2} + \dot{E}_{1\text{-gen}} + \dot{E}_{1\text{-conv}} + \dot{E}_{1\text{-rad}} \quad (1)$$

$$\dot{E}_{2\text{-sys}} = \dot{E}_{2\text{-TEC}} + \dot{E}_{2-3} + \dot{E}_{2-1} + \dot{E}_{2\text{-gen}} + \dot{E}_{2\text{-conv}} + \dot{E}_{2\text{-rad}} \quad (2)$$

$$\dot{E}_{3\text{-sys}} = \dot{E}_{3\text{-TEC}} + \dot{E}_{3-1} + \dot{E}_{3-2} + \dot{E}_{3\text{-conv}} + \dot{E}_{3\text{-rad}} \quad (3)$$

where the numbers (1, 2, and 3) correspond to the first stage, the second stage, and the rim, respectively, $\dot{E}_{i\text{-sys}}$ ($i = 1, 2, 3$) represents the rate of energy storage in the i^{th} thermal mass (the first stage, the second stage, and the rim; see Fig. 1C), $\dot{E}_{i\text{-TEC}}$ is the rate of heat transfer from the i^{th} thermal mass to the thermoelectric-cooler surface due to conduction by air, \dot{E}_{i-j} ($i, j = 1, 2, 3$, but $i \neq j$) is the rate of heat transfer from the i^{th} thermal mass to the j^{th} thermal mass due to conduction, $\dot{E}_{i\text{-gen}}$ is the rate of heat generation by the microheaters, $\dot{E}_{i\text{-conv}}$ and $\dot{E}_{i\text{-rad}}$ are the rates of heat transfer from the i^{th} thermal mass to the ambient due to natural convection and radiation, respectively. In addition, we apply a constant voltage pulse, V_i , to the microheater on the i^{th} stage using a power supply, while the electrical resistance of the microheater on the i^{th} stage, R_i , changes linearly

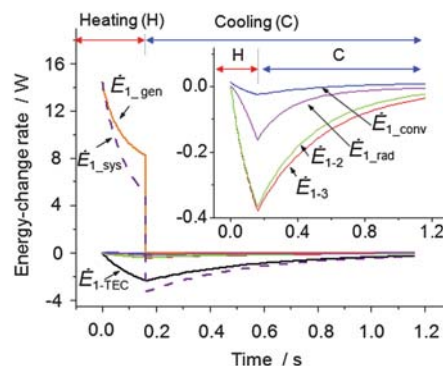


Fig. 2 Energy-change rates at the μ TM first stage. The values are calculated from the energy balance for each subcomponent. The input voltage is a square pulse of 40 V with duration of 150 ms. The air gap, the Pyrex thickness, and the IC length are 38 μm , 100 μm , and 1 mm, respectively. The energy-storage rate of the first stage ($\dot{E}_{1\text{-sys}}$) balances with the other energy-transfer/generation rates. When the heat is generated at the heater of the first stage ($\dot{E}_{1\text{-gen}}$), it is mainly dissipated through the thermoelectric cooler ($\dot{E}_{1\text{-TEC}}$). The inset shows that the heat dissipated through the other paths (conduction to the second stage and to the rim (\dot{E}_{1-2} and \dot{E}_{1-3}); convection and radiation to the environment ($\dot{E}_{1\text{-conv}}$ and $\dot{E}_{1\text{-rad}}$), respectively) is insignificant.

with temperature, T (ESI, Fig. S2†). Thus, the heat generation term can be written as follows:

$$\dot{E}_{i_gen} = V_i^2 / R_i(T) \quad (i = 1, 2) \quad (4)$$

Fig. 2 shows the time evolution of each energy rate in the first stage based on our model, when its microheater is turned on for 0.15 s at 40 V. The energy-storage-rate term (\dot{E}_{1_sys}) balances with the heat-transfer terms and the sign of each energy-rate term has the following meaning: the sign of the \dot{E}_{1_sys} value reflects the sign of the first-stage temperature-change with time, because \dot{E}_{1_sys} is proportional to the temperature-change rate ($\dot{E}_{1_sys} \propto dT/dt$); the heat-transfer terms take positive values when thermal energy moves into the first stage. The model assumes that the thermoelectric cooler is left on to maintain its temperature at approximately -55°C throughout the entire process. \dot{E}_{1_gen} is initially at its maximum and decreases during the heating process as the electrical resistance of the microheater increases with time (or alternatively with temperature) while the applied voltage remains constant. So, we define the average heating power as the time integration of \dot{E}_{1_gen} over the heating time that the applied DC voltage is on divided by the time. Notably, \dot{E}_{1_TEC} is the dominant heat-dissipation term among the heat-transfer terms. As shown in the inset of Fig. 2, heat conduction through the Pyrex membrane and the ICs (\dot{E}_{1-3} and \dot{E}_{1-2}) is more important than convection and radiation (\dot{E}_{1_conv} and \dot{E}_{1_rad}). The two terms, \dot{E}_{1-3} and \dot{E}_{1-2} , in conjunction with the heat transfer *via* the air gap (\dot{E}_{i_TEC}) affect the thermal crosstalk between the two stages. Compared with the other heat-transfer terms that initially have a value of zero, \dot{E}_{1_conv} and \dot{E}_{1_rad} have small positive values at the outset because of the difference between the ambient temperature (25°C) and the initial temperature of the first stage (-55°C). Thus, in convection and radiation, thermal energies initially move into the first stage.

Effect of Pyrex thickness on thermal response

To efficiently trap the eluting vapors and introduce them to the second-dimension column in a narrow band, fast cooling and heating are necessary with low heating and cooling power. We focused on minimizing thermal-response time and heating power. For practical reasons related to microfabrication, we focused on Pyrex-membrane thicknesses of 40 and 100 μm , and compare the experimental data and the theoretical prediction. Initially, the μTM was approximately at -55°C by the cooling unit. When a constant voltage was applied for a 150 ms duration, the first stage heated up and reached its maximum temperature; then it cooled down to -55°C (Fig. 3A and 3B). As expected, the device with the thinner Pyrex membrane was raised to a higher temperature for a given applied voltage. It required only 62% of the average power required for the thicker-membrane device (*i.e.*, 6.8 W *vs.* 11 W) to achieve a temperature of 200°C (Fig. 3C). For the experimental data, the time evolution of power was directly measured from the applied current and the voltage and, for the theoretical prediction, it was calculated from the electrical resistance and the voltage at the microheater. Then, the average heating powers were obtained from the area of heating power curve (*e.g.* \dot{E}_{1_gen} curve in Fig. 2) divided by the duration of the voltage pulse (*i.e.*, 150 ms). The thinner Pyrex membrane

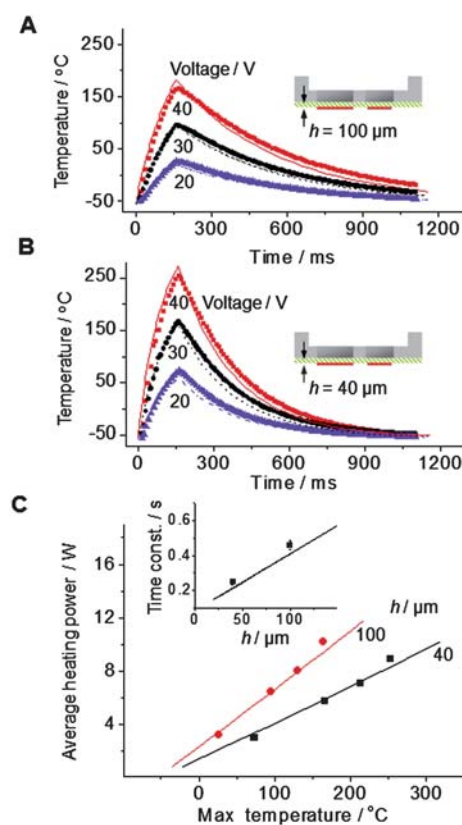


Fig. 3 Thermal response of the μTM first stage as a function of input voltage-pulse for Pyrex membrane thicknesses, h , of (A) 100 μm and (B) 40 μm (points: experimental data, lines: theoretical predictions). The input voltage was a square pulse with duration of 150 ms. The air gap and the IC length are 38 μm and 1 mm, respectively. The thinner (40 μm) Pyrex membrane results in faster cooling and a higher temperature at the same applied voltage. (C) Average heating power and its corresponding maximum temperature. The average heating power is defined as the area of the \dot{E}_{1_gen} curve divided by the duration of the voltage pulse (150 ms). The μTM with the thicker (100 μm) Pyrex membrane requires higher power to achieve the same maximum temperature. The inset shows the time constant³⁰ of the μTMs as a function of h .

also permits a faster cooling response (Fig. 3A and 3B), with the time constant (τ) for cooling being about half of that for the device with the thicker Pyrex membrane (*i.e.*, $\tau = 0.24$ *vs.* 0.46 s, Fig. 3C inset).³⁰

The inset of Fig. 3C shows a linear relationship between τ and the membrane thickness. The τ is proportional to the thermal mass (M_T) and is inversely proportional to the thermal conductance (G_T) by the heat-transfer terms (*i.e.* $\tau = M_T / G_T$). The Pyrex-membrane thickness generally affects both M_T and G_T . Even though the values of \dot{E}_{1-3} and \dot{E}_{1-2} change with the Pyrex thickness, G_T shows little change because \dot{E}_{1_TEC} , which is only governed by the air-gap size, is the dominant term in the heat transfer (Fig. 2). As a result, the change of τ is mainly dependent on M_T . Thus, τ is linearly proportional to the Pyrex thickness.

Effect of air gap on thermal response

We then explored how changing the air-gap thickness affects the heating and cooling responses of the device. Fig. 4A shows the

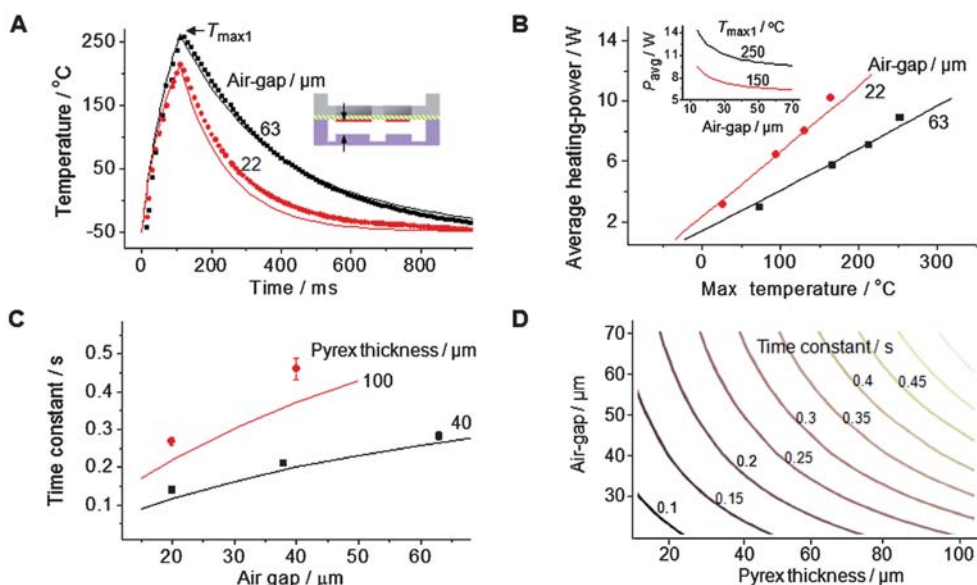


Fig. 4 Thermal response of the first μ TM stage influenced by the air gap (points: experimental data, lines: theoretical predictions). Here, the Pyrex thickness, the IC length, and the duration of the input voltage-pulse are 40 μm , 1 mm, and 100 ms, respectively. (A) Results for different air-gap sizes. The applied voltage peak is fixed at 35 V. The narrower air gap results in a lower maximum temperature but faster cooling. (B) Average heating power and its corresponding maximum temperature. The narrower air gap requires higher power for the same maximum temperature. The inset shows a nonlinear relation between the theoretical average heating-power (P_{avg}) and the air gap. (C) Influence of air gap and Pyrex thickness on the time constant. As the air gap becomes narrow, the time constant becomes smaller, *i.e.*, faster thermal response. (D) Theoretical contour lines of the time constant with respect to the various combinations of the air-gap and the Pyrex-thickness values.

thermal response of the first stage for two representative air gaps (22 μm and 63 μm) upon applying 35 V to the microheater for 100 ms. Notably, the temperature increase was smaller for the device with the smaller air gap. Accordingly, the power required to reach a maximum temperature of 210 $^{\circ}\text{C}$ was calculated to be 11.5 W with the smaller air gap and 7.2 W with the larger gap (Fig. 4B). The inset of Fig. 4B shows that the theoretical average heating-power required for reaching the same maximum temperature of the first stage (T_{max1}) increases sharply with the decreasing air gap.

On the other hand, the narrower air gap resulted in faster cooling (Fig. 4A). Fig. 4C clearly shows variations of τ with the air-gap size for devices with two different Pyrex membrane thicknesses. The change in τ with the air gap is more pronounced for the device with the 100- μm membrane. However, the values of τ tended to converge as the air gap became small for both membrane thicknesses. Fig. 4D summarizes the values of τ predicted for various combinations of the Pyrex thickness and the air gap. Here, we see that a narrow air gap enhances the cooling speed at the expense of higher heating power. Initially setting the air gap small (down to 22 μm) is a practically viable approach because (1) once we set the system, it is difficult to change the air-gap size while the power can be easily controlled and (2) the power consumption is found to be still at an acceptable level even for the narrow air gap of 22 μm .

Although τ varies linearly with the Pyrex-membrane thickness (inset of Fig. 3C), it varies nonlinearly with the air gap (Fig. 4C). This nonlinear relation comes from the relation between the thermal conductance, G_T , and the air gap. The G_T can be thought of as $a/L_{\text{air}} + b$, where a and b are constants, because the rate of the heat transfer *via* the air gap ($\dot{E}_{\text{I-TEC}}$) varies inversely

proportional to the air-gap thickness (L_{air}) while the other heat transfer terms are invariant. Thus the result is $\tau \propto 1/G_T = 1/(a/L_{\text{air}} + b)$. Fig. 4C also shows a steeper slope of the time-constant curve for the larger Pyrex thickness. Because τ is also proportional to M_T , the thicker Pyrex membrane makes the slope of the time-constant curve steeper.

Effect of air gap and IC length on thermal crosstalk

Although the heating of one of the stages inherently influences the temperature at the other stage (Fig. 5A), this thermal crosstalk should be minimized to independently control the temperatures of the two stages. To achieve this goal, we varied the air gap from 22 to 38 μm and the IC length from 0.5 to 1.5 mm based on theoretical modeling and experimental data indicating that these would provide a reasonable tradeoff between thermal-response speed and heating-power consumption, and would also provide acceptable vapor-modulation performance. Specifically, an air gap >40 μm yielded a cooling time from 250 to -50 $^{\circ}\text{C}$ of >1 s, while an air gap <20 μm required >13 W to heat from -55 to 250 $^{\circ}\text{C}$ (inset of Fig. 4B). Also an IC longer than 1.5 mm may result in broader vapor peaks because of the large temperature gradient inside the IC.

As shown in Fig. 5B, the IC length affects the thermal crosstalk more than the air-gap thickness in these ranges. For a first-stage maximum temperature (T_{max1}) of 200 $^{\circ}\text{C}$, the maximum temperature rise of the second stage (ΔT_{max2}) varied from 9 to 11 $^{\circ}\text{C}$ with the air gap varying from 22 to 38 μm for the IC length fixed at 1.5 mm, whereas ΔT_{max2} changed from 9 to 19 $^{\circ}\text{C}$ with the IC length varying from 1.5 mm to 0.5 mm with the air gap fixed at 22 μm . We see that the thermal crosstalk, which is defined

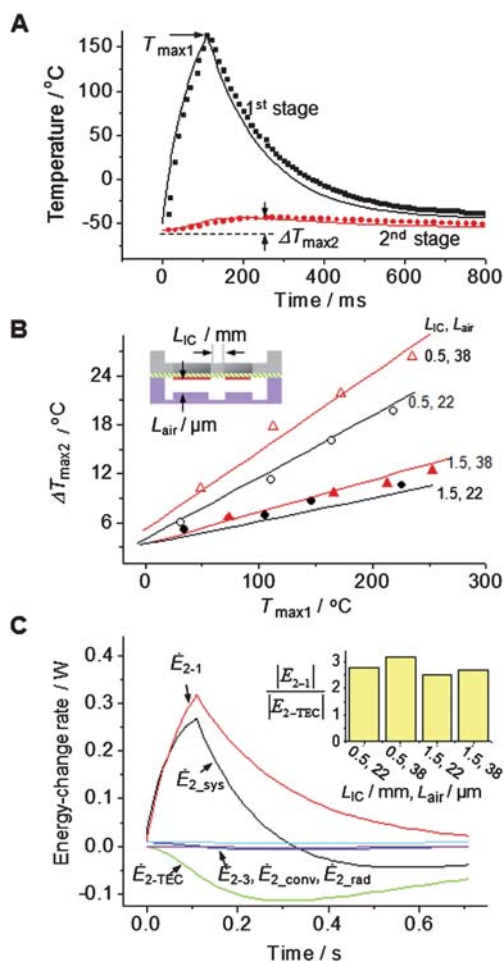


Fig. 5 Thermal crosstalk between the two μ TM stages (points: experimental data, lines: theoretical predictions). The duration of the input voltage-pulse and the Pyrex thickness are 100 ms and 40 μ m, respectively. (A) Temperature rise of the second stage by the heating of the first stage. T_{max1} is the maximum temperature of the first stage, and ΔT_{max2} is the maximum temperature rise of the second stage. The air-gap, the IC length, and the applied voltage-pulse are 22 μ m, 1 mm, and 35 V, respectively. (B) Influence of air-gap and IC length on ΔT_{max2} . (C) Energy-change rates at the second stage by the heating of the first stage. The air gap (L_{air}), the IC length (L_{IC}), and the square voltage-pulse applied to the first stage are 38 μ m, 1.5 mm, 40 V with 100 ms duration, respectively. The inset shows the ratio of the energy dissipated through the IC (\dot{E}_{2-1}) and through the air-gap (\dot{E}_{2-TEC}) over the time for the temperature rise to reach ΔT_{max2} .

as $\Delta T_{max2}/\Delta T_{max1} \times 100\%$, was maintained as small as 9.2% (at $T_{max1} = 200$ °C) even for the worst case where the IC length and the air gap were 0.5 mm and 38 μ m, respectively.

The dominant effect of the IC length on the thermal crosstalk can be explained by comparing dissipated thermal energies. The energy-storage rate of the second stage (\dot{E}_{2-sys}) balances with the other heat-transfer parameters (Fig. 5C). However, \dot{E}_{2-1} and \dot{E}_{2-TEC} , which originate from the conductive heat transfer between the two stages *via* IC and between the second stage and the thermoelectric cooler *via* the air gap, respectively, are the major contributors to the temperature of the second stage. So we consider only these two terms for our analysis. We estimated the effects of the air gap and the IC length on the maximum

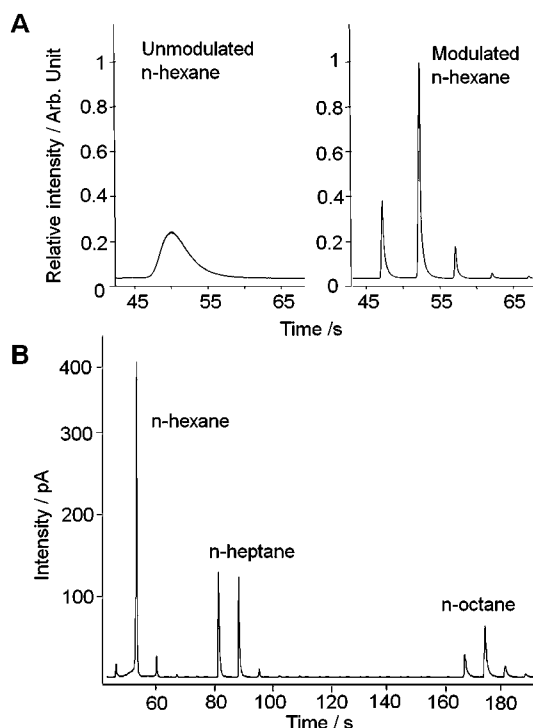


Fig. 6 Modulation of injected test samples using a μ TM with a 22- μ m air gap, a 100- μ m Pyrex membrane thickness, and a 1-mm IC length. Square voltage-pulses of 40 V and 35 V were applied to the microheaters on the first and second stage, respectively, for 100 ms each at 1 s delay. (A) Comparison of unmodulated and modulated FID responses for two separated injections of n-hexane. The modulation period was 5 s. There is an enhancement in relative intensity and a reduction in peak width for the modulated peaks. (B) Modulated peaks of an injected headspace sample of a mixture of n-hexane, n-heptane, and n-octane vapors, using a modulation period of 7 s. The relative magnitudes of the peaks and their FWHM values reflect the relative volatility of the mixture components.

temperature rise of the second stage (ΔT_{max2}) by considering dissipated energies rather than energy-change rates, because ΔT_{max2} represents an energy state determined by the thermal history. Thus, we compared the ratio of the two dissipated energies (\dot{E}_{2-1} , \dot{E}_{2-TEC}) at ΔT_{max2} . The energies were calculated by integrating the area of \dot{E}_{2-1} and \dot{E}_{2-TEC} curves, respectively. Regardless of the values used for the IC length and air gap, the ratio of the two dissipated energies remain at a value of ~ 3 (inset of Fig. 5C), indicating that the IC length dominates the thermal crosstalk.

Peak modulation

Initial tests of the μ TM operation were successful. A device with a 100- μ m-thick Pyrex membrane, a 22- μ m-thick air gap and a 1-mm-long IC was used. The homologous series of alkanes, n-hexane, n-heptane, and n-octane, was used to span a moderate range of volatility (vapor pressures range from 14–140 mmHg at 25 °C) while retaining symmetric peak shapes with the upstream separation column operated at 30 °C. n-Hexane was used for single-vapor testing. The modulator was operated in the range of -30 °C to 250 °C. Heating and cooling rates were 2800 °C s $^{-1}$ and -250 °C s $^{-1}$, respectively.

Unmodulated, the injected sample of n-hexane, gave a broad, low-intensity peak with a full-width half-height (FWHH) value of 4.1 s. With an identical second injection and modulation period of 5 s, the μ TM generated 5 n-hexane peaks with FWHH values of 0.3 s that collectively elute in the same amount of time as the unmodulated peak (Fig. 6A). Although a shorter modulation period would lead to a greater number of modulated peaks, it is generally considered sufficient to generate 3 slices of each initial (unmodulated) peak passing through a modulator.³¹ The expected resolution enhancement is reflected in the decrease in the FWHH value, which, in this case is ~ 14 -fold; narrower peaks are more easily resolved by the second dimension column in a GC \times GC system. This, in turn, increases the overall peak capacity. As expected, there is an increase in the maximum peak height upon modulation as well. Here, a ~ 5 -fold peak enhancement is achieved in the height of the largest modulated peak relative to that of the unmodulated peak. This would result in a commensurate decrease in the limit of detection. Of course, the maximum signal and FWHH values will be affected by the modulation period, heating and cooling rates, and velocity of the carrier gas through the modulator. The results shown here serve to illustrate that initial testing shows the μ TM is operating as expected.

Fig. 6B shows the chromatogram of the alkane mixture with a 7 s modulation period. As in Fig. 6A, there was a 1 s delay between heating the two μ TM stages. The relative magnitudes of the signals are qualitatively consistent with the theoretical headspace concentration of each component, which is a function of their vapor pressures, and the FWHH values of 0.26, 0.37, and 0.70 s, for n-hexane, n-heptane, and n-octane, respectively, also reflect the relative volatility of the components. Although there is some evidence of breakthrough for n-hexane, as indicated by the apparent increase in the baseline at the base of the largest modulated peak, it is clear that the μ TM is effectively focusing and desorbing all three mixture components. Breakthrough of less volatile compounds can be reduced or eliminated by reducing the modulation period, increasing the stage length, or reducing the injected sample mass.¹³ These issues are a matter of optimizing the device design and the operating conditions relevant to a particular analysis. With the μ TM employed for these tests, cooling from 250 to -20 °C requires ~ 0.9 s, which limits the minimum modulation period and the delay between heating the stages to no less than 1 s. Reducing this period any further would increase the extent of breakthrough observed for the more volatile compounds in a mixture. This limitation is due largely to the relatively thick Pyrex-membrane used in this device. Designs with thinner membranes should reduce this problem and allow for more rapid temperature cycling.

Conclusions

We have developed and tested a MEMS-based μ TM, designed for use in comprehensive two-dimensional separations of complex mixtures of volatile organic compounds. Two significant advances over the existing TMs include (1) fast thermal response at a low heating power (~ 10 W), where the power is two orders of magnitude smaller than that of the conventional benchtop TMs, and (2) no need for cryogenic consumables for cooling. These unique features constitute a significant advantage

over current TM techniques. Also, the thermal crosstalk between the two stages was negligible ($<9\%$), thereby enabling independent control of their temperatures. Furthermore, a lumped thermal model provided predictions in remarkably good agreement with the experimental results. The model predicted the temperatures of each stage and included all heat transfer modes of the μ TM system. As a result, the model enabled quantitative analysis on the thermal response and thermal crosstalk of each stage as the Pyrex-membrane thickness, the air gap, and the IC length were varied. Although we confined this thermal model for the analysis of the μ TM, the model could be applied to any thermal systems when the thermal mass and heat transfer terms are properly considered. Finally, using a set of n-alkane test compounds, we demonstrated the capability for enhancing analytical sensitivity and chromatographic resolution with the μ TM.

Ongoing work is focusing on more in-depth studies of the separation of volatile organic compounds with the μ TM integrated in a conventional benchtop GC setup. In the near future, we will integrate the μ TM with μ GC columns^{20–26} to develop a μ GC \times μ GC system. Such a microsystem would enable the on-site detection of complex gas-mixtures at various locations such as industrial plants, hospitals, airports, and agricultural fields. In this paper, we have taken a significant step towards the realization of comprehensive μ GC \times μ GC by demonstrating the first MEMS-based μ TM.

Acknowledgements

This work was supported by NASA under the grant No. NNG-06GA89G. This work made use of Engineering Research Centers Shared Facilities supported by the National Science Foundation under Award Number EEC-0096866. The authors would like to thank Katharine Beach for her advice and assistance in device fabrication, and also appreciate the help of staffs at the Lurie Nanofabrication Facility for device fabrication.

References

- 1 J. Dalluge, J. Beens and U. A. T. Brinkman, *J. Chromatogr., A*, 2003, **1000**, 69–108.
- 2 T. Gorecki, J. Harynuk and O. Panic, *J. Sep. Sci.*, 2004, **27**, 359–379.
- 3 R. C. Y. Ong and P. J. Marriott, *J. Chromatogr. Sci.*, 2002, **40**, 276–291.
- 4 C. A. Bruckner, B. J. Prazen and R. E. Synovec, *Anal. Chem.*, 1998, **70**, 2796–2804.
- 5 J. V. Seeley, F. Kramp and C. J. Hicks, *Anal. Chem.*, 2000, **72**, 4346–4352.
- 6 J. B. Phillips, D. Luu and J. B. Pawliszyn, *Anal. Chem.*, 1985, **57**, 2779–2787.
- 7 J. B. Phillips, R. B. Gaines, J. Blomberg, F. W. M. van der Wielen, J.-M. Dimandja, V. Green, J. Granger, D. Patterson, L. Racovalis, H.-J. de Geus, J. de Boer, P. Haglund, J. Lipsky, V. Sinha and E. B. Ledford, *J. High Resolut. Chromatogr.*, 1999, **22**, 3–10.
- 8 P. J. Marriott and R. M. Kinghorn, *Anal. Chem.*, 1997, **69**, 2582–2588.
- 9 R. M. Kinghorn, P. J. Marriott and P. A. Dawes, *J. High Resolut. Chromatogr.*, 2000, **23**, 245–252.
- 10 J. Beens, M. Adahchour, R. J. J. Vreuls, K. van Altna and U. A. T. Brinkman, *J. Chromatogr., A*, 2001, **919**, 127–132.
- 11 J. Harynuk and T. Gorecki, *J. Chromatogr., A*, 2003, **1019**, 53–63.
- 12 M. Adahchour, J. Beens and U. A. T. Brinkman, *Analyst*, 2003, **128**, 213–216.
- 13 M. Libardoni, J. H. Waite and R. Sacks, *Anal. Chem.*, 2005, **77**, 2786–2794.

- 14 M. Libardoni, E. Hasselbrink, J. H. Waite and R. Sacks, *J. Sep. Sci.*, 2006, **29**, 1001–1008.
- 15 S. C. Terry, J. H. Jerman and J. B. Angell, *IEEE Trans. Electron Devices*, 1979, **26**, 1880–1886.
- 16 A. de Mello, *Lab Chip*, 2002, **2**, 48N–54N.
- 17 C.-J. Lu, W. H. Steinecker, W.-C. Tian, M. C. Oborny, J. M. Nichols, M. Agah, J. A. Potkay, H. K. L. Chan, J. Driscoll, R. D. Sacks, K. D. Wise, S. W. Pang and E. T. Zellers, *Lab Chip*, 2005, **5**, 1123–1131.
- 18 P. R. Lewis, P. Manginell, D. R. Adkins, R. J. Kottenstette, D. R. Wheeler, S. S. Sokolowski, D. E. Trudell, J. E. Byrnes, M. Okandan, J. M. Bauer, R. G. Manley and C. Frye-Mason, *IEEE Sens. J.*, 2006, **6**, 784–795.
- 19 E. T. Zellers, S. M. Reidy, R. A. Veeneman, R. Gordenker, W. H. Steinecker, G. R. Lambertus, H. Kim, J. A. Potkay, M. P. Rowe, Q. Zhong, C. Avery, H. K. L. Chan, R. D. Sacks, K. Najafi, K. D. Wise, in *Proceedings of the Transducers'07*, Lyon, France, June 10–15, 2007, pp. 10–14.
- 20 S. Zampolli, I. Elmi, F. Mancarella, P. Betti, E. Dalcanale, G. C. Cardinali and M. Severi, *Sens. Actuators, B*, 2009, **141**, 322–328.
- 21 G. Lambertus, A. Elstro, K. Sensenig, J. Potkay, M. Agah, S. Scheuering, K. Wise, F. Dorman and R. Sacks, *Anal. Chem.*, 2004, **76**, 2629–2637.
- 22 G. Serrano, S. M. Reidy and E. T. Zellers, *Sens. Actuators, B*, 2009, **141**, 217–226.
- 23 A. D. Radadia, R. I. Masel, M. A. Shannon, J. P. Jerrell and K. R. Cadwallader, *Anal. Chem.*, 2008, **80**, 4087–4094.
- 24 M. Agah, J. A. Potkay, G. Lambertus, R. Sacks and K. D. Wise, *J. Microelectromech. Syst.*, 2005, **14**, 1039–1050.
- 25 S. Reidy, G. Lambertus, J. Reece and R. Sacks, *Anal. Chem.*, 2006, **78**, 2623–2630.
- 26 S. Reidy, D. George, M. Agah and R. Sacks, *Anal. Chem.*, 2007, **79**, 2911–2917.
- 27 B. H. Bae, J. Yeom, A. D. Radadia, R. I. Masel, M. A. Shannon, in *Proceedings of the Transducers'07*, Lyon, France, June 10–15, 2007, pp. 1497–1500.
- 28 J. J. Whiting, C. S. Fix, J. M. Anderson, A. W. Staton, R. P. Manginell, D. R. Wheeler, E. B. Myers, M. L. Roukes, and R. J. Simonson, in *Proceedings of the Transducers'09*, Denver, USA, June 21–25, 2009, pp. 1666–1669.
- 29 F. P. Incropera and D. P. DeWitt., *Introduction to Heat Transfer*, John Wiley & Sons, NY, 3rd edn, 1996.
- 30 The time constant (τ) is inherently determined by the given thermal mass and the thermal property of the material; it can be exactly estimated when the system can be described by the first order differential equation. In this case, time constant is defined as the required time to reach 63% of the steady-state value.
- 31 R. E. Murphy, M. R. Schure and J. P. Foley, *Anal. Chem.*, 1998, **70**, 1585–1594.